

LA-UR-13-22138

Approved for public release; distribution is unlimited.

Title: Ten Trials at Lower Slobbovia: Searching for Repetitive Electromagnetic and Seismoacoustic Signatures in Explosions

Author(s): Nemzek, Robert J.
Arrowsmith, Stephen J.
Layne, John P.

Intended for: Report for sponsor
Report



Disclaimer:

Los Alamos National Laboratory, an affirmative action/equal opportunity employer, is operated by the Los Alamos National Security, LLC for the National Nuclear Security Administration of the U.S. Department of Energy under contract DE-AC52-06NA25396. By approving this article, the publisher recognizes that the U.S. Government retains nonexclusive, royalty-free license to publish or reproduce the published form of this contribution, or to allow others to do so, for U.S. Government purposes. Los Alamos National Laboratory requests that the publisher identify this article as work performed under the auspices of the U.S. Department of Energy. Los Alamos National Laboratory strongly supports academic freedom and a researcher's right to publish; as an institution, however, the Laboratory does not endorse the viewpoint of a publication or guarantee its technical correctness.

Ten Trials at Lower Slobbovia: Searching for Repetitive Electromagnetic and Seismoacoustic Signatures in Explosions

LA-UR-13-nmnn

R.J. Nemzek

ISR-2, Los Alamos National Laboratory

S. J. Arrowsmith

EES-17, Los Alamos National Laboratory

J.P. Layne

ISR-3, Los Alamos National Laboratory

For additional information contact: Dr. Robert Nemzek, MS-B244, Los Alamos National Laboratory, Los Alamos, NM 87545; 505-667-0822; Nemzek@lanl.gov

Executive Summary

We performed a series of ten explosion tests, each test being a single 10-kg cylinder of Comp-B with a PBXN-9 booster. Eight of the tests were placed 2 m above ground level, one was at ground level, and one was 1 m below ground in a backfilled hole. The explosions were monitored by radio antennas to detect electromagnetic emissions and seismo-acoustic instrumentation. We found that certain aspects of the radiofrequency emission regimes repeated from test to test. Some features showed a systematic variation across tests, which we interpret as the effect of each detonation on the nearby ground. The radio emissions were probably from the high-temperature detonation shock, follow-on combustion, and frictional charging of dirt entrained by the blast. The below-ground test in particular generated an anomalously-high level of RF at both low and high frequencies, presumably due to the large amount of dirt and rock involved. The seismoacoustic observations clearly discriminate the buried shot from the table and surface shots, which appear as a single population. Seismoacoustic waveforms from repeating tests at local distances have highly self-similar waveforms but amplitudes are strongly dependent on atmospheric conditions. We show that we can correct for meteorological effects on amplitude for upward-refracting atmospheres, but that correction for downward-refracting atmospheric profiles requires a coupled correction for topography.

Purpose of Tests

The test series described here was designed as a joint effort between two DOE/NA-22/Weaponization projects, "Detonation-RF: Validation in Simulation" and "Detection and Characterization of Explosions Related to Weaponization: A Multi-Technology Approach." A combined seismo-acoustic and electromagnetic emissions measurement set had already been established for the latter project, to supply a variety of data combining both measurement phenomenologies, thereby generating a database suitable for developing a multi-phenomenology detection/classification algorithm. For the Detonation-RF problem, one of the key issues in interpreting the signal as signature is repeatability. Obviously, the repeatability, or lack thereof, is also of concern to the development of detection algorithms. Additionally, understanding coupling between blast and earth is vital for interpreting seismoacoustic data. With these factors in mind, we (Arrowsmith and Nemzek) determined that a series of 10 standardized explosions could fulfill requirements of both projects while remaining within a reasonable budget and execution time.

Test Series Description

A set of ten nominally identical charges were obtained from Accurate Energetic Systems LLC, McEwen, TN. Each charge (Figure 1) consisted of 10 kg of Comp-B cast in a Sonotube form, which was removed before delivery of the charges. The charges were evidently cast in a series of pours, as layering was evident in the final product. Sonotube is a commercially-available concrete form, basically a spiral-wound cardboard tube. It is treated with a plastic coating for waterproofing. This coating may have reacted slightly with the Comp-B, as a slight surface discoloration was noted [V.E. Sanders, personal communication, 2012)]. The nominal size of the Comp-B cylinders was 8" diameter by 8" high. To ensure high-order detonation, a 4" diameter x 1" thick PBXN-9 booster weighing 1.1 lb was epoxied to the Comp-B. A PBX-9407 pellet driven by an Exploding Bridge Wire (EBW) detonator initiated the assembly.



Figure 1. An assembled 10-kg Comp-B assembly on its shot stand.

The experimental design called for eight of the charges to be set 2 m above ground, providing a set of identical replicates. The 2-m height was selected to reduce the effects of ground interaction with the RF signals; those effects were expected to be due to ground-shockwave contact and the generation of ballistic or otherwise airborne dust and dirt. A simple wooden shot stand (Figure 2) was designed, consisting of a 2-m-tall "pyramid" formed from crossed 3/4" plywood members, topped by a horizontal table also of 3/4" plywood.

The final two charges were expended in singular tests for seismoacoustic calibration purposes: one was placed directly on the ground; the other was placed in a 1-m-deep hole and subsequently backfilled.



Figure 2. 10-kg Comp-B assembly and plywood shot stand in firing configuration.

The test area used at Lower Slobbovia (Figure 3) was an approximately 30 m x 30 m flat, open area surfaced with "sand," the sand being derived from the local Bandelier Tuff, i.e., volcanic ash. It is primarily a glassy silicate material, with minor quartz, sanidine feldspar (Gardner et al., *Rhyolites and associated deposits of the Valles-Toledo caldera complex, New Mexico Geology*, p. 3-18; 1, 32, 2010; and references therein). Within 1-2 feet of the surface, the loose material transitions into a fractured tuff (i.e., solid rock). Despite the dry conditions around LANL during the spring and summer of 2012, the subsurface rock and dirt were conspicuously damp. All ten shots were placed at the same location. After each elevated test (Figure 2), the remains of the plywood stand (Figure 4) were removed, the area flattened as needed, and a new stand erected in its place. The ninth shot was placed on the ground at the same location (Figure 5), and finally the area was excavated and backfilled for the 1-m-deep test (Figures 6 and 7). As can be seen in the pictures, the test range had a number of other objects in the vicinity of the explosions, primarily earth-covered bunkers, Jersey Bounce walls, and a few metal structures.



Figure 3. Lower Slobbovia. The red star indicates the approximate firing location for the series. The LANL antenna can be seen SE of the star in this May 2012 image, but occupied a spot more nearly west during the tests.

Each charge was detonated by a standard high-voltage fireset. Standard-video-rate imagery was recorded for most tests. For the above-ground tests, a plume of smoke and dust was generated; as implied above, much of the shot table collapsed onto the ground directly below the charge location, and essentially no crater formation was noted. The ground-level test generated a wide but shallow crater which involved only the surface dirt. The buried test resulted in a large plume of dirt and rocks, and generated a correspondingly deep and wide crater.



Figure 4. Aftermath of a 10-kg elevated test: the plywood stand has collapsed in place.



Figure 5. The ground-level shot.



Figure 6. The below-ground shot, wrapped in a plastic bag for protection from water.



Figure 7. The below-ground shot, backfilled and ready for firing.

Measurement Equipment Description

The RF signals generated during the test were recorded by a set of two antennas (Figure 8), an ADA-120 active dipole, and an SAS-230 active broadband discone, both manufactured by ARA Inc. The antennas were both vertically-oriented, and placed on a mast about 10 m above the test plane, at a slant range of about 45 m. The elevation angle of the antennas with respect to the detonations was therefore on the order of 15° . The antenna outputs were conditioned with a series of preamplifiers, filters, and attenuators (Figure 8). The signals were digitized at 2 GSa/s by two Acqiris 10-bit digitizer cards. The digitizers were triggered by the "T0" trigger. The digitizers recorded 500 MSa per channel, with a 50% pretrigger. Therefore, the timeseries for each channel included 125 ms of pre-shot background, and 125 ms of post-shot signal. A 1-ms delay was placed between the T0 trigger and the fireset trigger pulse itself, leading to a detonation at $T+1\text{ms}$. This extra delay was not an experimental requirement. For clarity, the extra delay has been removed from all data and results reported here; in other words, Zero-Time within this report is the time that the fireset pulse was emitted. With about 30 m of detonator cable between the fireset and charge, and an unknown function time for the bridgewire itself, the detonation commenced slightly after $T=0$.

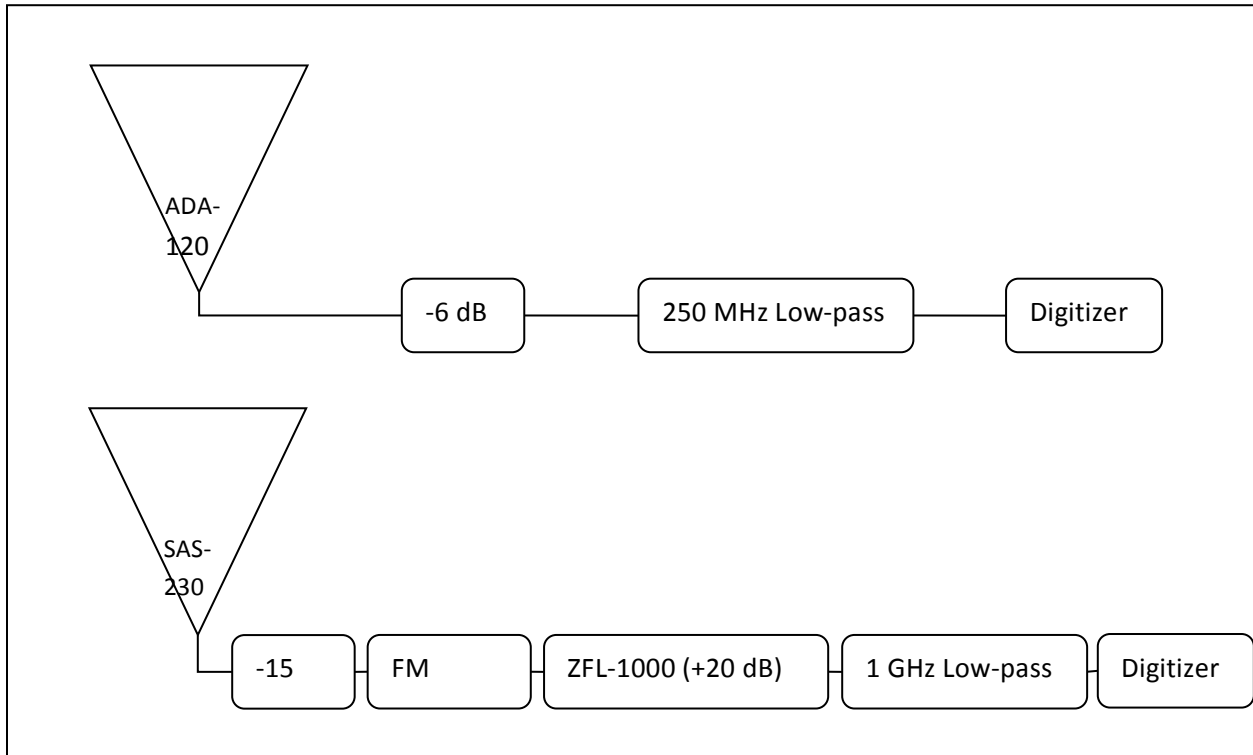


Figure 8. Signal conditioning for the two RF channels.

The raw timeseries records of the ten tests all show clear RF generated by the detonation. We have also processed the data through an empirical carrier-removal (Fourier filtering) process to maximize the number of RF pulses detected. The resulting data are shown as digitizer voltages, i.e., without correction for gains and antenna factors. Data from Test 1 is the exception to this rule: recording parameters were identical for Tests 2-10, but Test 1 was recorded with 6 dB higher gain. The extra gain has been mathematically-removed in data shown here, resulting in amplitudes that can be directly compared among the ten tests. However, the reduced dynamic range available for Test 1 may affect the ability of our data processing to extract information, and so not all parameters derived for Test 1 should be considered directly comparable to Tests 2-10.

Several seismoacoustic sensor sites were selected for these experiments in order to characterize both source and path effects. Sensors at the different sites varied but included Reftek data acquisition systems, external GPS clocks, broadband seismometers (deployed in vaults with thermal insulation at PLDY, LOSL and LSAR - see the map in Figure 9), low-frequency acoustic sensors (fitted with porous hoses for wind noise reduction at more distant sites), solar panels and car batteries for power. Seismoacoustic sensor deployments from all 10 tests are shown in Figure 9, there were five separate locations where sensor systems were deployed.

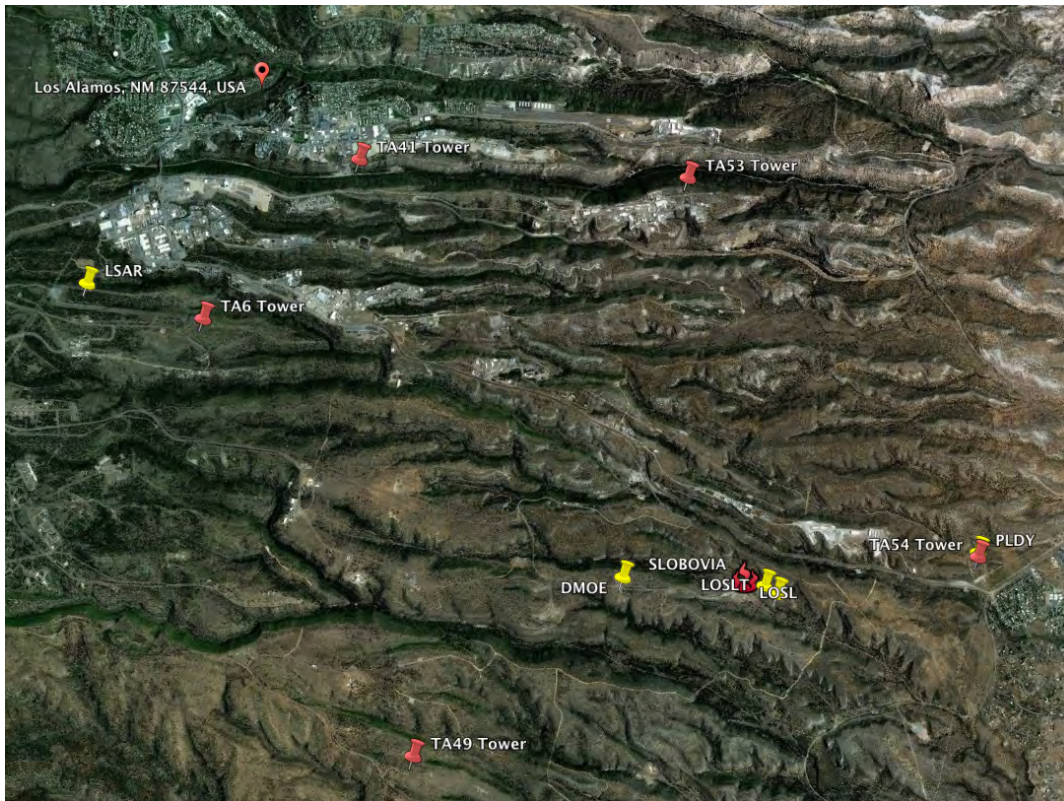


Figure 9. Map showing the locations of the SLOBOVIA test (fire symbol), seismoacoustic sensor deployments (yellow pins), and meteorological towers (red pins). Stations LOSL and LOSLT are located just to the east of the SLOBOVIA test. Station PLDY is collocated with the TA54 meteorological tower.

At each site, acoustic sensors were arranged in arrays to enhance the signal to noise ratios using beamforming. Arrays were designed by considering the dominant frequency content of signals measured from previous explosion tests conducted at the LANL firing sites. The acoustic array at PLDY was designed to have an optimal response that covered the frequency range from 0.5 - 40 Hz. Figure 10 shows the theoretical array response of the array at PLDY for different array configurations. The array configuration chosen is shown in the bottom right panel in Figure 10. The array at LSAR consisted of four microphones, separated by ~ 100 m, while arrays at DMOE, LOSL, and LOSLT comprised short-aperture (high-frequency) arrays of three sensors with aperture of ~ 10 m.

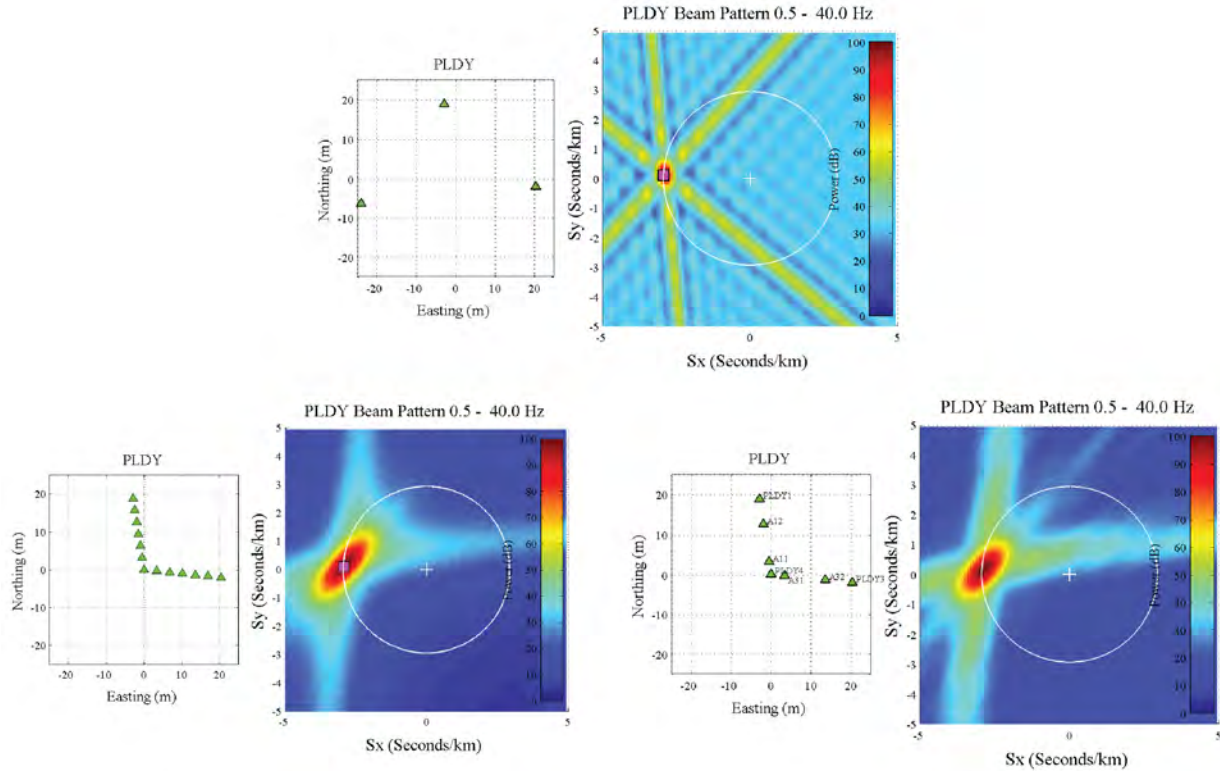


Figure 10. Theoretical response functions for a vertically arriving wave with frequency content of 0.5 – 40 Hz for different array geometries (each green triangle represents an individual microphone. The top response, which is calculated for a typical triangular array geometry, shows significant aliasing, which is reduced by adding more sensor nodes (bottom panel).

Analysis of Radiofrequency data

CDU Peak Group

All datasets have a distinct feature associated with the high-voltage pulse from the Capacitive Discharge Unit (CDU). We show this for the first eight tests in Figure 11. This is the low-frequency antenna; the high-frequency channel shows a similar feature, although it is less reproducible. The CDU feature begins at $T+0.93 \mu\text{s}$ in all channels, and is complete by $T+8 \mu\text{s}$. This assures us that all data records are synchronized to within a small fraction of a microsecond, and that the CDU feature does not contaminate the true explosion RF occurring later in the record. The CDU feature has many features that reproduce with high fidelity in each successive test. Presumably these could be related to the fireset, the detonator cable, and the EBW itself, but we have not attempted to determine the origin of any specific details.

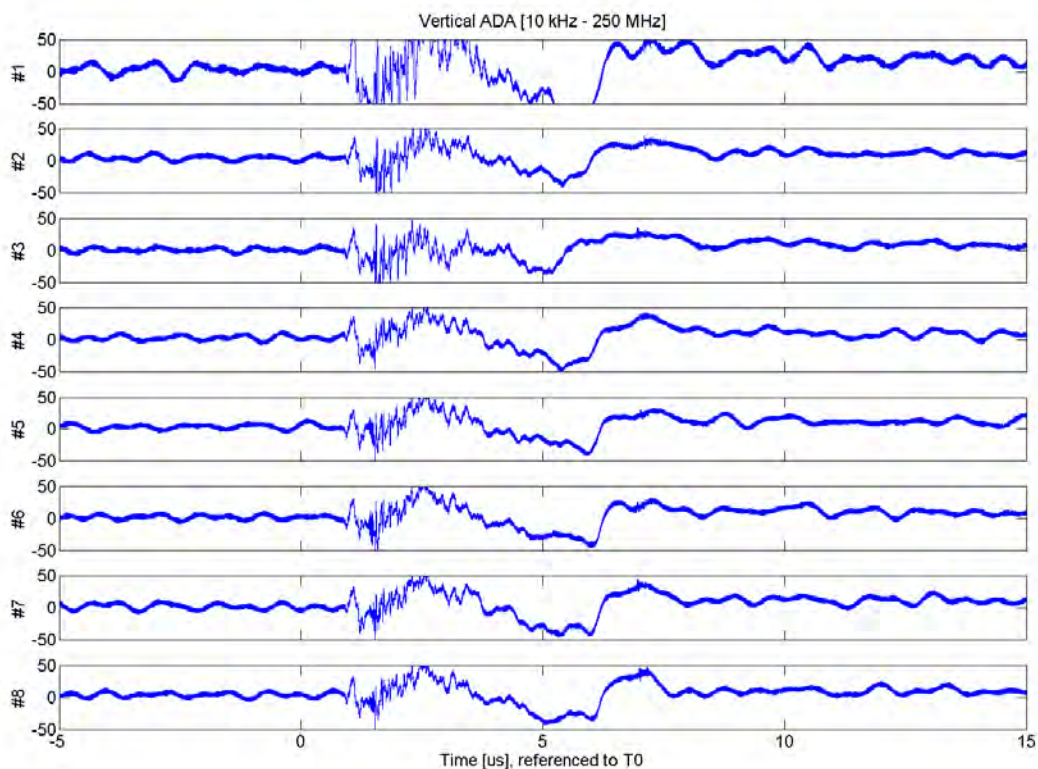


Figure 11. CDU pulse in eight identical tests.

30 μ s Peak Group

In the remainder of our discussion of the eight identical tests, we focus on the high-frequency channel (20MHz – 1 GHz), as very little RF shows up in the low-frequency channel. Following the CDU feature, all eight tests generated a brief set of RF pulses at $25.4 \pm 1.8 \mu$ s (Figure 12). The repetitive envelopes seen in most of the records are modulated radio carriers. For later processing, these carriers were removed by Fourier filtering. This was followed by several robust bursts of RF, at varying times in each record, but centered around 30 μ s. These 30 μ s bursts are somewhat different from the typical explosion RF expected, as they are relatively long. Following the 30 μ s bursts, there are sporadic RF pulses for the next 2 ms, as described below. We treat the 30 μ s group separately, as they may be predicted by simulation. Raytheon model calculations for an isolated 10 kg Comp-B cylinder show that the electric field components (static, inductive, and radiative) start to increase after about 30 μ s, reaching a peak near 60 μ s, and continuing until approximately 120 μ s (Figure 13, provided by H. Choe, J. Edmiston, and C. Vannatta of Raytheon Network Centric Systems). Thus, the emissions from the tests, starting at 25 μ s, may be identical to those predicted by the model. However, the emission in the data does not show any tendency to increase to a peak at 60 μ s. The Raytheon simulations show that the highest temperatures and pressures reached during the detonation at the bottom of the cylinder, i.e., in the direction of the detonation wave, where the shock builds up. We postulate that the intense temperatures and pressures in this region were effectively damped out by interaction with the plywood shot table, much of which was simply forced downward by the force of the explosion, thereby reducing the amount of RF generated.

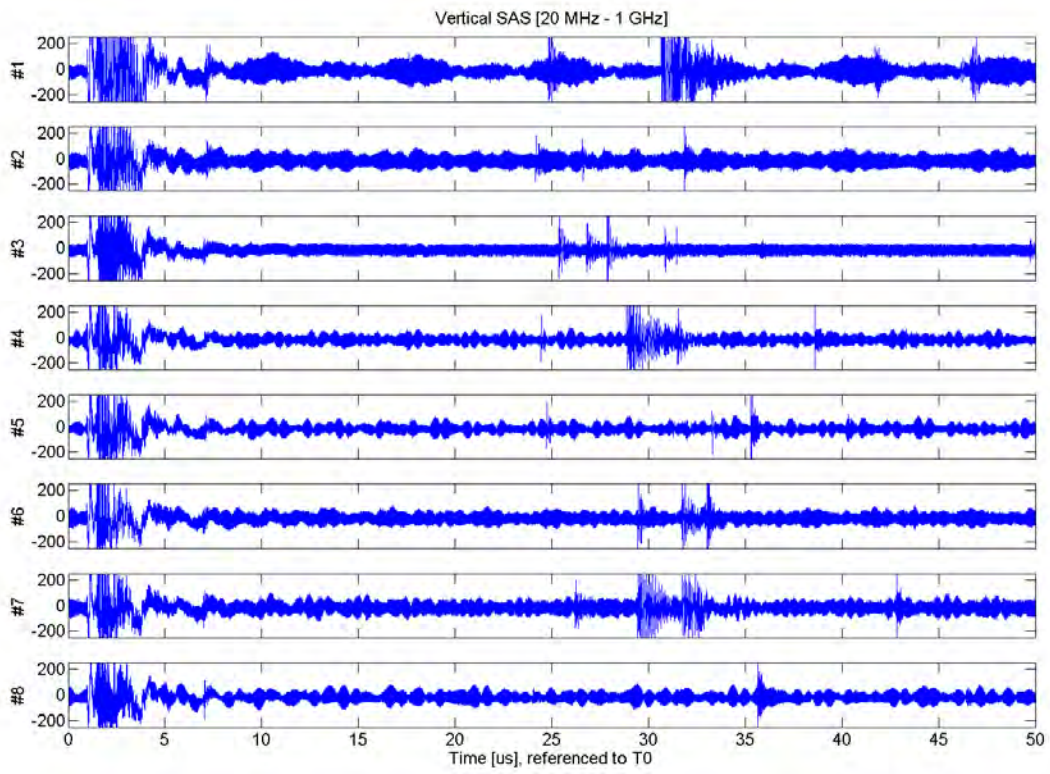


Figure 12. First 50 microseconds of the eight elevated tests: all eight start to produce RF at $T+ 25 \mu\text{s}$.

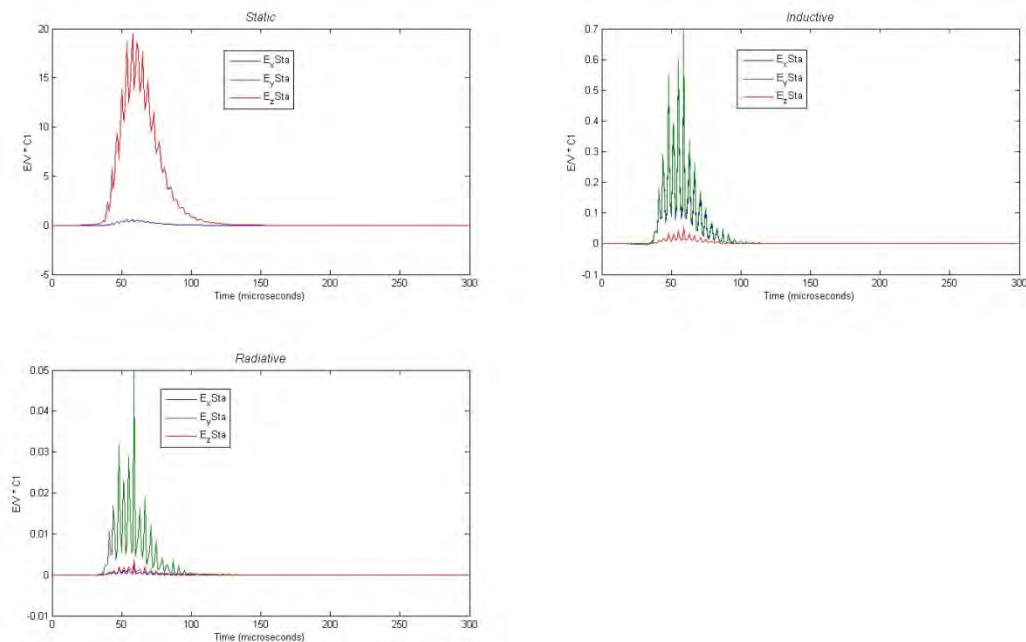


Figure 13. 3-axis Static, Inductive, and Radiative field components predicted for a 10-kg Comp-B charge in free space, according to Raytheon model calculations. The fields start to rise at $T+ \sim 30 \mu s$, and continue until about $T+ 100 \mu s$.

1 ms Peak Group

The first two milliseconds of the eight datasets show a sporadic generation of RF, mostly contained within the first millisecond post-detonation (Figure 14). This emission is quite variable from test to test, except for the $30 \mu s$ discussed above. For example, Test 5 appears to have generated almost no RF after $T+50 \mu s$, while Test 6 generated a large amount of RF throughout the first millisecond but almost none afterwards, and Test 8 generated significant bursts of RF in both the first and the second millisecond. Every test produced a peak pulse rate between $400 \mu s$ and $800 \mu s$. In a free-field situation, the shock wave was calculated to reach the ground at $T+410 \mu s$. This is identical to the earliest peak following the detonation signature, leading us to the conclusion that the emissions between 400 and $800 \mu s$ are due to ground contact, either through direct grounding of charge or via a piezoelectric effect. Presumably the shock wave or detonation byproducts were slowed or deflected in most of the tests by the presence of the plywood stand, resulting in the variation in time of the ground contact pulse. After $T+2$ ms, no additional RF emission occurred in any of the eight tests for an additional several milliseconds. Explanations of the RF generation must also account not only for the presence of emissions, but also for the presence of this distinct gap.

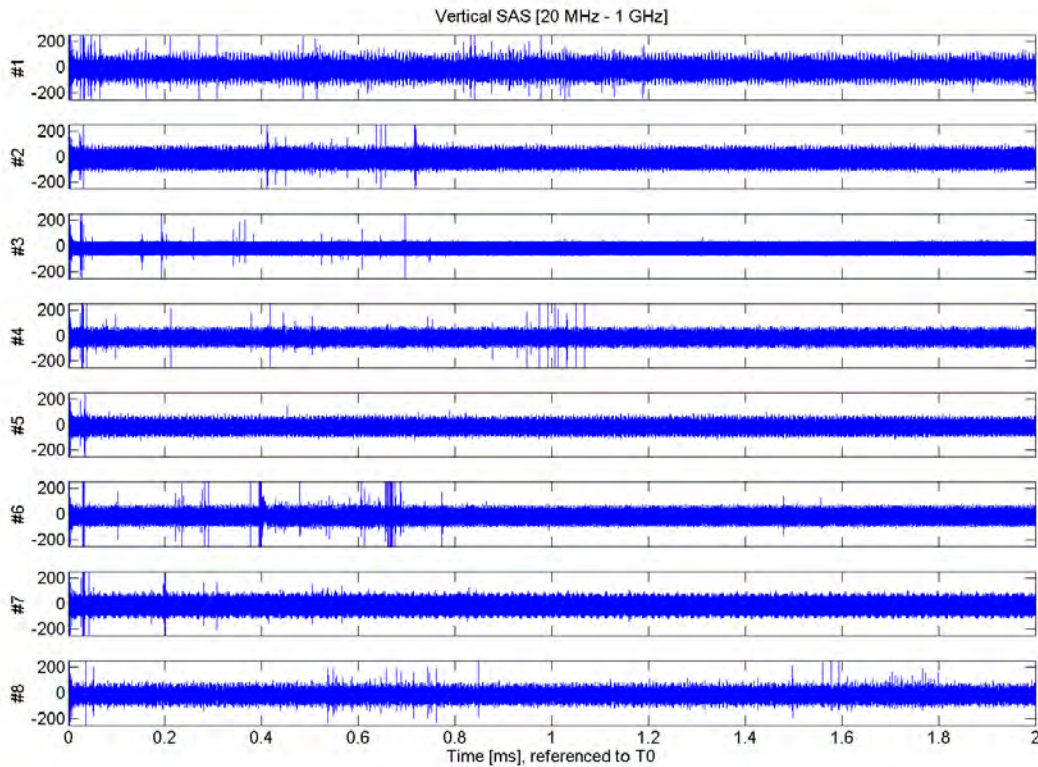


Figure 14. RF emission for the first 2 ms of the eight tests. All spikes rising above the overall baseline of each test were generated by the explosions.

5 ms Peak Group

In Figure 15 we present recordings of the first 15 ms of all eight tests. We see that the emission for all but one test temporarily ends after 1 ms, and that all emissions end after 3 ms. There is then a gap until at least $T+5$ ms, at which time sporadic emission restarts in Test 4, and all tests have restarted by $T+8$ ms. It is difficult to make any quantitative assessment of the spiky, quasi-random emissions, so we convert the data into a more understandable form: the rate plot. The rate plot summarizes the statistical properties of the data, which is necessary for interpreting a quasi-random process.

Figure 16 shows an example rate plot for the entire data set, from $T-126$ ms to $T+124$ ms. To make this plot, the data were first passed through the Fourier-filter process, which removed carrier signals in the timeseries. The data were then passed through an algorithm which identified every individual peak above a certain threshold. The threshold was adjusted empirically to find the level at which the pre-shot background generated about one spurious peak per millisecond. This was then used to process the entire test, identifying the peak amplitude and time for each RF pulse. The peaks times were then reduced to a rate by counting the number within a 1-ms-wide window, which was slid across the timeseries at 0.1 ms resolution. The use of the sliding window broadens any features in the data, and in particular can make the RF signal appear to start before $T=0$.

In the rate plot, we see the very low pulse rate before the test, then the $T=0$ burst followed by a second burst near 5 or 10 ms, and a die-off to a rate which is low but still distinctly higher than the pre-test background.

In Figure 17, we zoom in to the first 50 ms of the test. Three zones are highlighted. First, the red encompasses everything within the first two milliseconds. This zone includes the CDU pulse and other features described above; due to the inclusion of the CDU, the height of this peak should not be taken as indicative of the explosion-RF per se. The blue zone will be discussed below. The green zone shows a group of emissions that appears in several records at nearly the same time, and may represent a distinct type of emission, i.e., it may have a distinct origin. This group is especially prominent in Test 1. We make no conjecture about the mechanism behind this “5-ms” group. It may well simply be part of the following region of rapid emission.

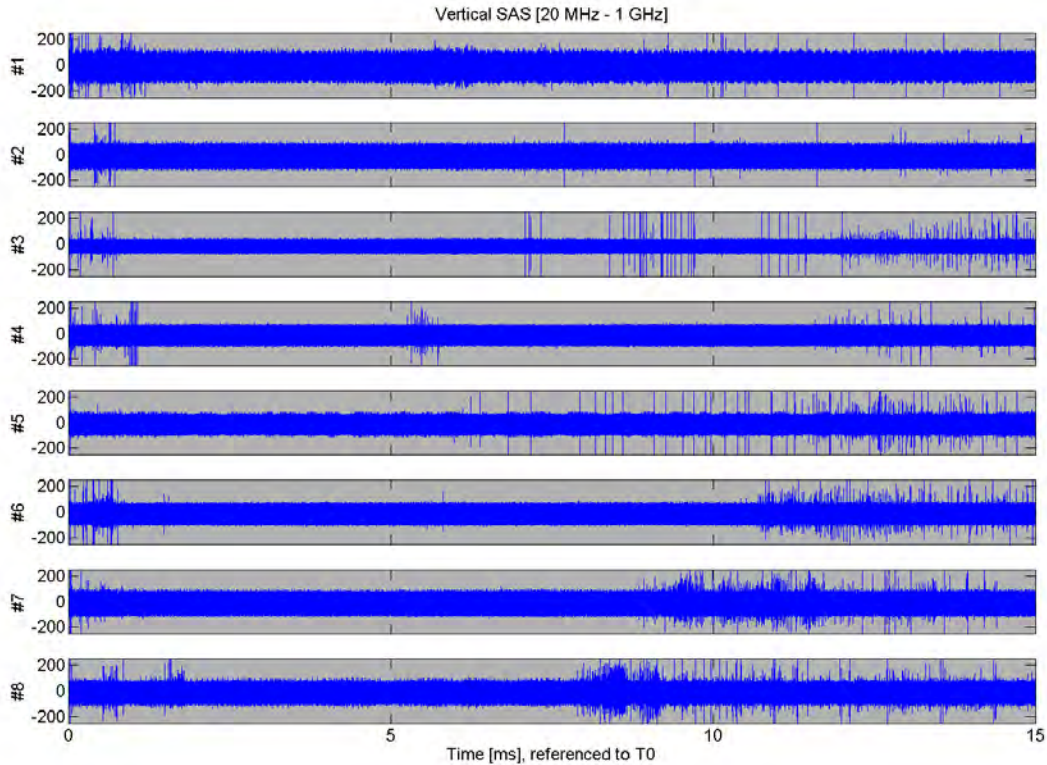


Figure 15. Emissions during the first 15 ms for the eight elevated tests. After T+2 ms, there is a conspicuous emission gap in all records until T+5 ms or later.

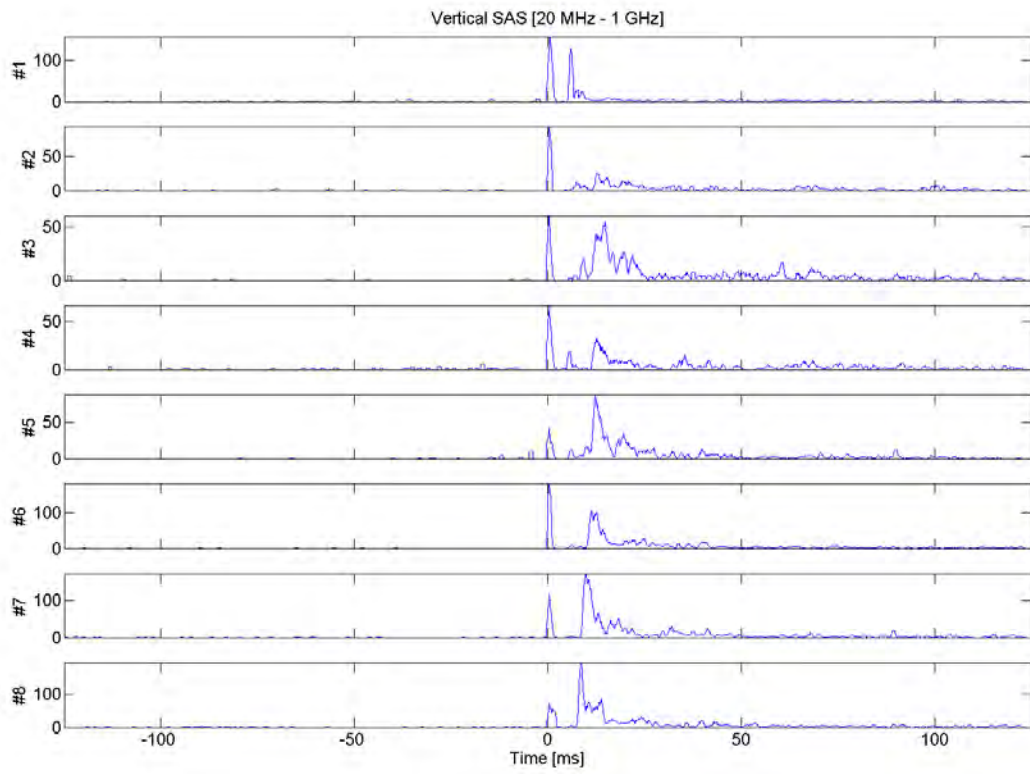


Figure 16. "Rate Plot" showing pulse emission rates per millisecond for all eight tests, for the entire recording period, from T-126 ms through T+125 ms.

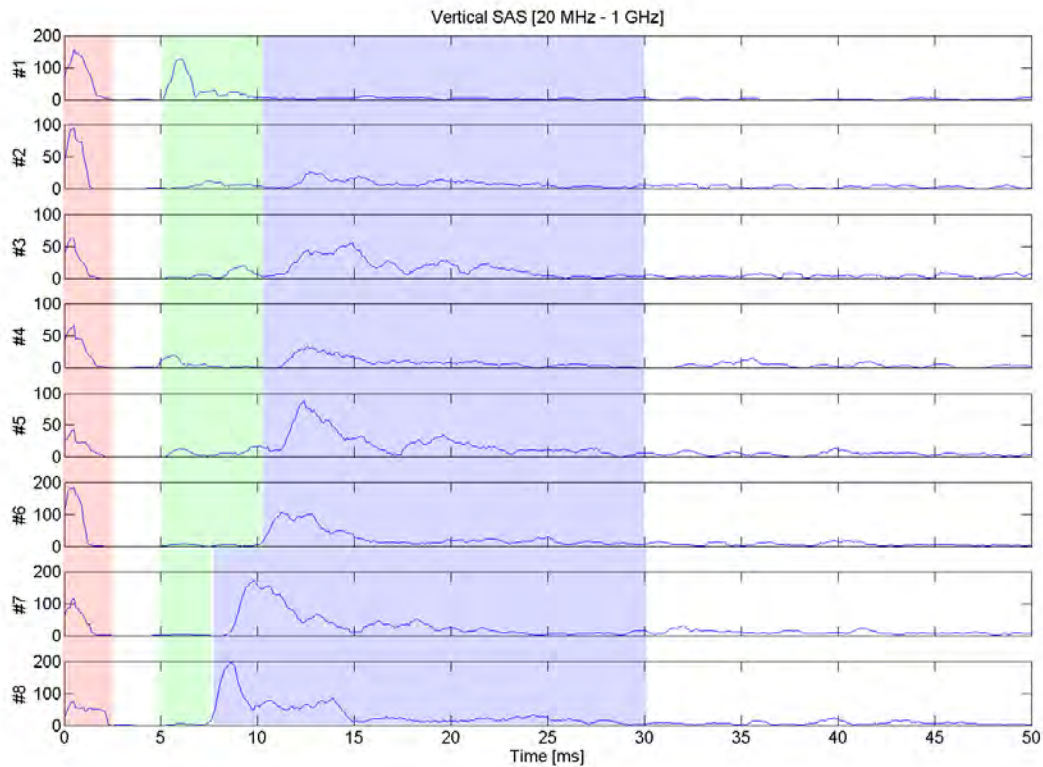


Figure 17. Rate Plot for the first 50 ms of all eight elevated tests. Common emission time regimes are color-coded.

10 ms Peak Group

The most distinct feature in the High-Frequency rate plots (Figure 17) is a peak with a rapid rise and slow decay that occurs near $T+10$ ms, highlighted in blue. This peak rises from zero to its peak in ~ 1.3 ms. It then decays back to near-background levels over approximately 20 ms, although the rate remains elevated above background for the remainder of the record. (Using $T+30$ ms as the duration of this feature is clearly an arbitrary decision.) This feature encompasses most of the RF spikes, and therefore most of the RF energy, emitted during the test. Close inspection of the 10-ms peak reveals that it changes systematically from test to test: progressing from Test 1 to Test 8, it becomes taller and arrives earlier. Figures 18 and 19 show this effect; although there is some scatter, clearly the time of the peak and its maximum amplitude change monotonically. Individual 10-ms features sometimes have multiple peaks; we have plotted the overall maximum. The peaks for each test mostly have similar shapes and durations, and therefore we would expect that the integrated energy would also increase with test. Using the processed data shown in Figure 20 (discussed below), we have subtracted the cumulative pulse count at $T+5$ ms from the cumulative pulse count at $T+30$ ms. This difference is very close to the integrated pulse count across the 10-ms peak. The results are shown in Figure 20; while there is more scatter than in Figure 19, the trend showing higher pulse counts for later tests remains.

The eight tests involved identical charges on identical shot stands. There is no compelling reason to suspect that detonation or combustion effects would vary systematically from test to test. The tests were performed on two days (Day 1: Tests 1, 2, and 3; Day 2: Tests 4, 5, 6, 7, and 8) with similar weather conditions and at

similar times of day. The five tests on Day 2 were all conducted within a few hours, some within 20 minutes of each other. If environmental conditions were involved, we might expect either a difference between Day 1 and Day 2, or a difference progressing from Test 1 to Test 3, and again from Test 4 through Test 8. We would not expect Tests 1 through 8 to form a continuous series. The aspect of the test conditions that might be expected to vary systematically with test number is the ground under the charge, as all tests were conducted in essentially the same location. We speculate that the shock striking the ground near the charge altered the soil conditions in some way the enhanced the amount of RF generated, and that by implication the bulk of the 10-ms peak and subsequent continuing RF is related to dust and dirt involved in the explosion. Each detonation may have compacted the ground beneath it; however, the ground surface was raked as part of the post-test cleanup. Perhaps the shock interaction with the ground broke down the preexisting soil particles, leaving more fine material available for charging interaction in each subsequent test. Another possibility is that the explosions changed the soil moisture and therefore its conductivity. We saw a similar phenomenon in 2006, when tests during successive weeks showed a dramatic change in the timing of late, low-frequency signals. Then, drenching rains between tests saturated the ground, and late signals moved forward in time. They appeared to be moving back to their original timing in successive tests, as the soil dried out. (We note that Tests 4 through 8 form a tighter association, and that the tests may in fact form two groups corresponding to the two days. Still, we believe that the underlying cause is the effect of the explosions on the ground, rather than independent environmental changes, primarily due to the short time between tests 4-8.)

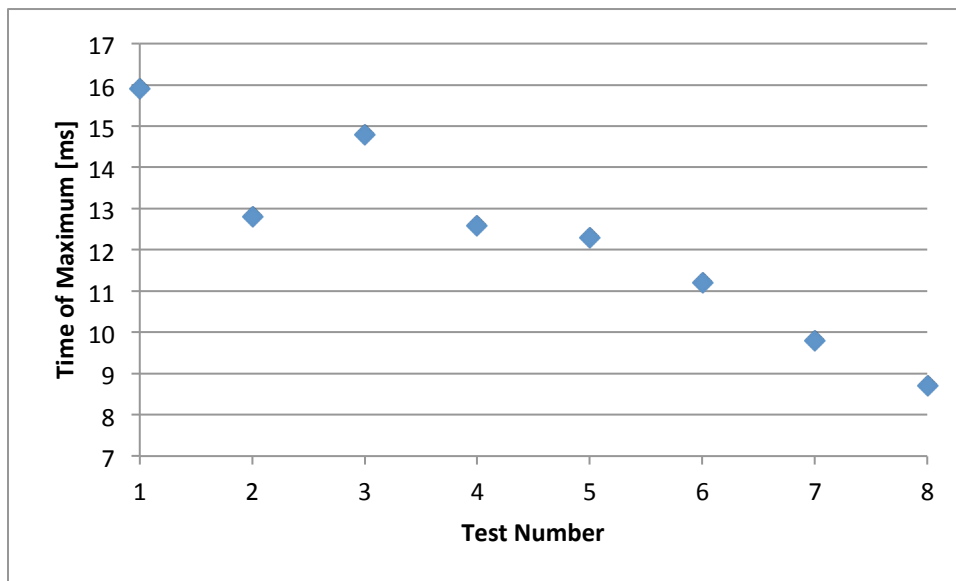


Figure 18. Time of maximum rate in "10-ms Peak Group." With each test, the feature peaked earlier. Times are referenced to T0.

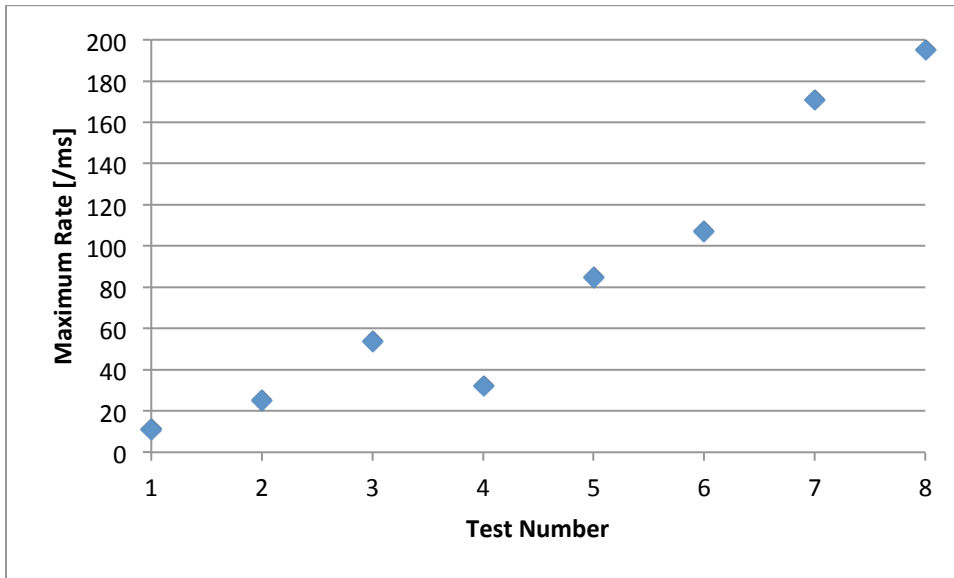


Figure 19. The maximum rate of each "10-ms Peak Group." With each test, the feature reached a higher maximum rate.

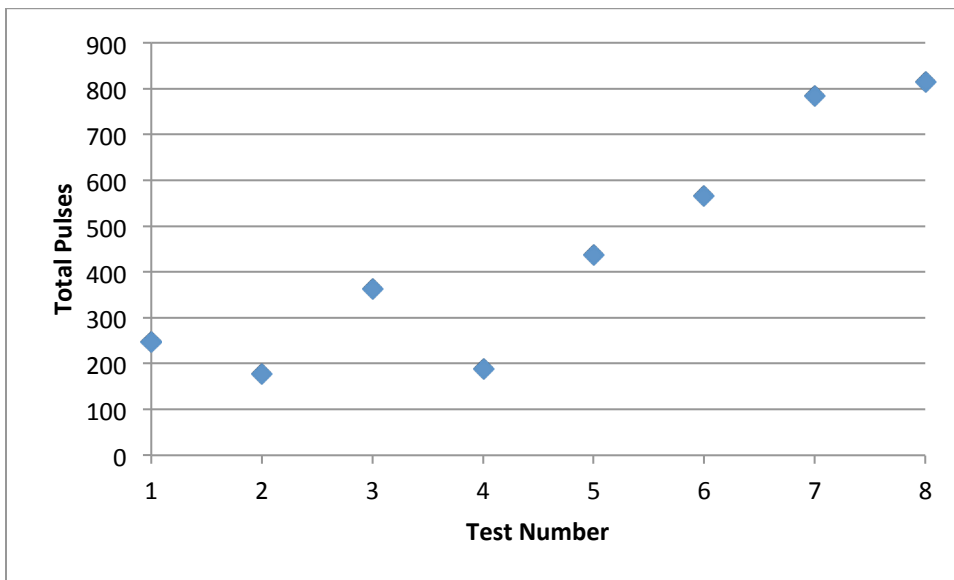


Figure 20. Cumulative pulse number in each "10-ms Peak Group." With each test, the integrated number of pulses in the peak grew larger.

100 ms Blast Effects

Propagation calculations for the blast wave from a 10-kg, 2-m-high Comp-B charge, show that the blast wave should arrive at a 45-m slant range in approximately 110 ms [Sanders, V.E., personal communication, 2012]. In each test, the RF background shows a distinct, low-frequency sine wave starting at 100-110 ms. We interpret this as motion of the antenna mast after arrival of the blast wave. Data after this point should be interpreted with care.

Total RF Production

We have found a number of similarities in the time histories of the eight tests. We now explore the total number of RF pulses generated in each event. Figure 21 is a cumulative sum of pulses detected as a function of time. We do not show Test 1 in this plot; the different dynamic range employed in that recording makes detailed comparison with the other tests problematic. In Tests 2-8, then, we see a slow rise in the pulse count before each test, reflecting the low background, then a step at, and just after, $T=0$, due to the CDU and the first 2 ms of RF emission. The major step in the curves is the 10 ms peak. The differing times of the step again show the effect of the 10-ms peak's transition to earlier times with each test. After the large step, the curve flattens, ending with a slope that is steeper than the pre-test slope, again indicating the enhanced pulse generation rate even 125 ms after the test. Overall, we see a factor of 2.8 difference in total pulse count between the lowest-emitting tests (#2 and #4) and the highest (#7 and #8). In several cases (2&4, 3&5, and 7&8), two tests generated very similar time histories, at least when expressed as cumulative pulse counts.

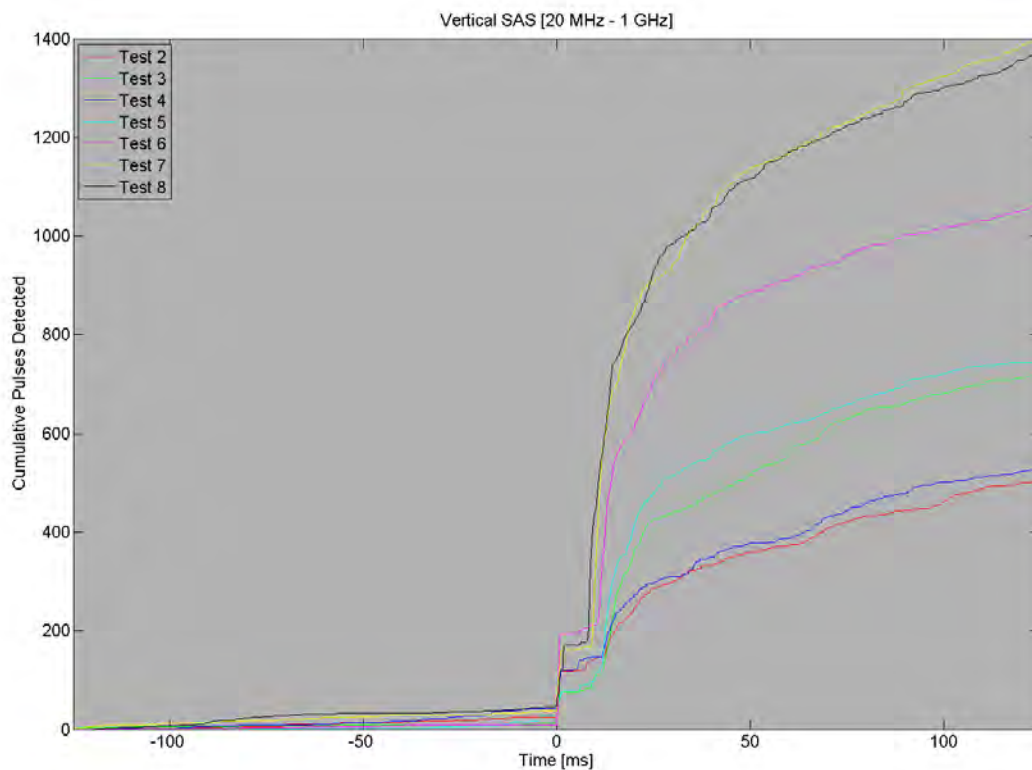


Figure 21. Cumulative pulse count for elevated tests 2 through 8.

Tests at Varying Heights

Tests 9 and 10 were intended to explore seismic coupling of the 10-kg Comp-B sources. However, they also generated highly interesting RF results. Shot #9 was placed directly on the ground, and created a shallow crater (Figure 22). The crater was approximately 225 cm diameter and 20 cm deep, with a central depression 38 cm diameter reaching 53 cm total depth. We estimate the total excavated volume to be

0.5 m³. This estimate does not account for the raised rim of the crater. It is clear that a large amount of material was ejected only a short distance, by the thick covering of smooth dirt around the crater, out to perhaps one crater diameter from the rim. All of the material in and around the crater appeared dry.

Test 10 was buried in a narrow hole to a depth of 1 m, then backfilled. The resulting crater (Figure 23) was approximately 390 cm diameter and 130 cm deep. Estimating the shape as a simple cone, we derive an excavated volume of 5.2 m³. The ejecta included a large number of pieces of broken pumice, some of them many meters from the explosion. Much of the ejected material was clearly wet.

Figures 24 and 25 present timeseries information from tests 6, 9, and 10. We chose Test 6 as the 2-m-high test for comparison to the 0-m-high and (-)1-m-test because it occurred very close to the same time of day the previous day as Test 9, and therefore should minimize any effects from the ambient environment. For these tests we show both low-frequency and high-frequency data; we have not shown any low-frequency recordings previously, as the amount of RF generated in the low frequency channel was minimal. Tests 6 and 9 both have the 30- μ s feature discussed earlier. That feature, however, is absent from Test 10. We assume that this is a result of the burial of the charge, and that either the detonation temperatures were suppressed due to the overburden, that the lack of air resulted in little or no ionization, or that any RF generated was attenuated by the overburden. Test 10, on the other hand, has a feature at 45-50 μ s that has little or no counterpart in the other tests; the coincident feature in Test 9 may, in fact, just be coincidental. This feature in Test 10 is relatively slow, having a characteristic frequency of about 1 MHz. From previous tests, we associate such slow features, albeit at later times, with static charging, presumably of dirt.

In Figures 26 and 27, we present rate plots for Tests 6, 9, and 10. For convenience in direct comparison, we have plotted all three tests on a common set of axes. The plots start at T-25 ms to expand the timescale somewhat; the preceding 100 ms of background were identical to the final 25 ms shown.

In the low frequency regime, Test 6 (+2 m) shows only a short burst of radiation near T+7 ms, and an even smaller burst near T+15 ms. Test 9 generated little to no RF in this band. Test 10 (-1 m), however, shows a very large peak starting near T+7 ms and peaking near T+18 ms. It has a second broad peak centered near T+45 ms, and a substantial tail continuing until the end of the record at T+125 ms. In the low frequency band, then, Test 10 is completely different from any other test. We note that the high pulse rates achieved in this test violate some assumptions of our peak-counting algorithm, perhaps leading to a systematic undercounting; therefore, the actual pulse rates could be substantially higher than calculated.

In the high frequency regime, we see again that Test 10 generated much more radiation than the other two tests. Test 6 had the 3rd-highest RF of the eight +2 m trials; Test 10 would easily stand out among all of the 10 trials. In addition to the two major peaks, Test 10 also shows a 3rd minor peak at about T+3 ms. Once again, the start of the primary peak in each test walks inward with test number: the largest radiation peak from Test 10 starts before Test 9, which itself starts before Test 6. We note that the peak of Test 10 arrives after the peak of Test 9; it may be that the “walking in” effect is appropriate for the small side peak on the left side of the main Test 10 peak, which in turn could argue that the excessive amount of radiation emitted by Test 10 was generated by a different mechanism than the smaller peaks in the other tests.

From the Rate Plots just shown and the Cumulative Pulse Count plots (Figures 28 and 29), we can derive the following quantities:

	Test 6 (+2 m)	Test 9 (0 m)	Test 10 (-1 m)
Highest Rate, Low Frequency	37 [/ms]	7 [/ms]	240 [/ms]
Highest Rate, High Frequency	107 [/ms]	61 [/ms]	308 [/ms]
Total Number of Pulses, Low Frequency	195 (147*)	167 (-35*)	3893
Total Number of Pulses, High Frequency	867	613	3130
Number of Pulses in Main Peak, Low Frequency	101 (91*)	54 (14*)	2388
Number of Pulses in Main Peak, High Frequency	565	410	2461
Number of Pulses in Secondary Peak, Low Frequency	94 (56*)	113 (-47*)	1505
Number of Pulses in Secondary Peak, High Frequency	302	198	669
<i>Pulses for $T < T+5$ ms subtracted in all calculations</i>			
<i>Main Peak = $T+6$ ms - $T+30$ ms</i>			
<i>Secondary Peak = $T+30$ ms - $T+125$ ms</i>			
<i>*with estimated cumulative noise subtracted</i>			

Table 1: Pulse Rates and Counts for Tests 6, 9, and 10.

We have defined the primary peak as all pulses occurring between $T+5$ ms and $T+30$ ms, and the secondary peak as all pulses occurring after $T+30$ ms. In this case, the use of 30 ms as a dividing line is justified, as it is the time of the minimum between the primary and secondary peaks. The calculations include data out to $T+124$ ms; there is no significant change in the pulse rate after $T+100$ ms (the time at which the blast wave affects the antennas). The pulse counts for the low-frequency channel in Tests 6 and 9 are fairly low compared to integrated background levels, so we have supplied numbers corrected for background as well as the raw counts, under the assumption that the pre-trigger background rate continued throughout the record. The other Tests and channels have high enough counts that such a correction would have minimal effect. We now ratio all of these numbers to those from Test 10:

Quantities in Ratio to Test 10	Test 6 (+2 m)	Test 9 (0 m)
Highest Rate, Low Frequency	0.15	0.029
Highest Rate, High Frequency	0.35	0.20
Total Number of Pulses, Low Frequency	0.050 (0.038*)	0.043 (0*)
Total Number of Pulses, High Frequency	0.28	0.20
Number of Pulses in Main Peak, Low Frequency	0.043 (0.038*)	0.023 (0.059*)
Number of Pulses in Main Peak, High Frequency	0.23	0.17
Number of Pulses in Secondary Peak, Low Frequency	0.062 (0.037*)	0.075 (0*)
Number of Pulses in Secondary Peak, High Frequency	0.45	0.30
<i>Pulses for $T < T+5$ ms subtracted in all calculations</i>		
<i>Main Peak = $T+6$ ms - $T+30$ ms</i>		
<i>Secondary Peak = $T+30$ ms - $T+125$ ms</i>		
<i>*with estimated cumulative noise subtracted</i>		

Table 2: Pulse Rates and Counts for Tests 6 and 9, normalized to Test 10.

We see that while the Highest Rate measure for the low-frequency channel in Test 6 is within a factor of 7 of Test 10, all cumulative low-frequency measures for both Tests 6 and 9 are over a factor of ten less than

corresponding measures for Test 10. The high-frequency metrics are less extreme, but still are typically 4-5x less than corresponding Test 10 numbers.



Figure 22. Crater resulting from the ground-level test: a substantial amount of ejected material remained near the crater, as indicated by the erasure of footprints.



Figure 23. Crater generated by the below-ground test: note the large and small rocks that now cover the sandy ground. The ejected material is darker than the ground surface due to its being wet.

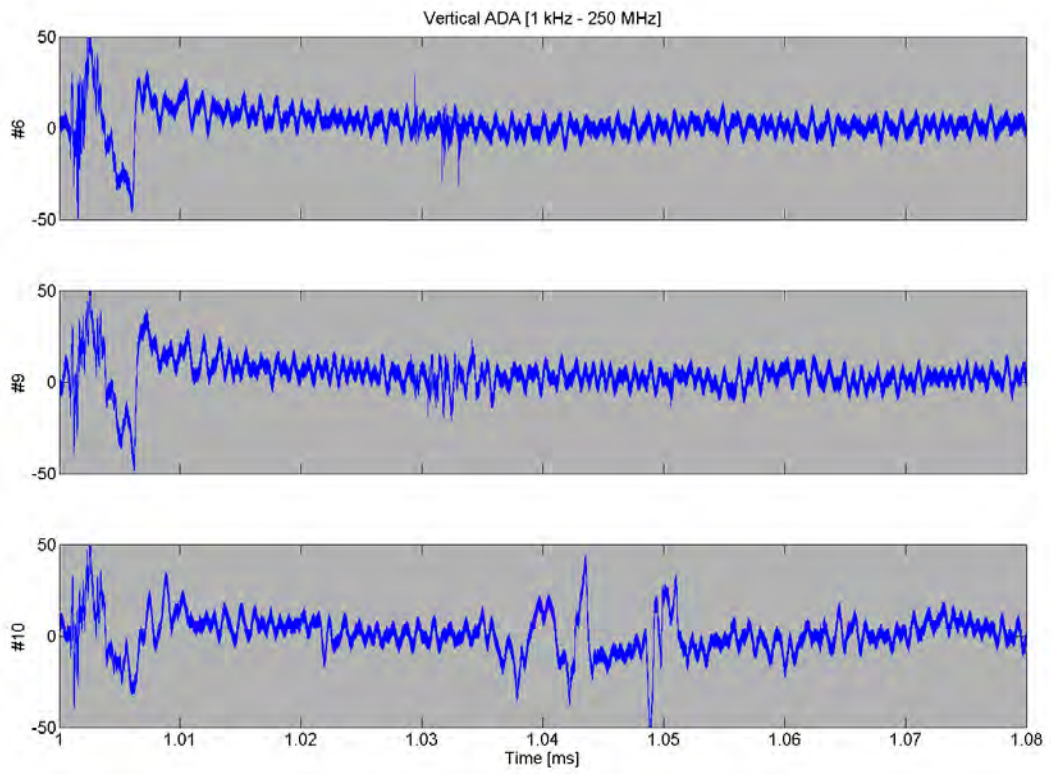


Figure 24. First 80 μs of Tests 6, 9, and 10, low-frequency antenna. Note that the 3 μs feature seen in the above ground tests is absent in Test 10, replaced by a slower feature at 40-50 μs .

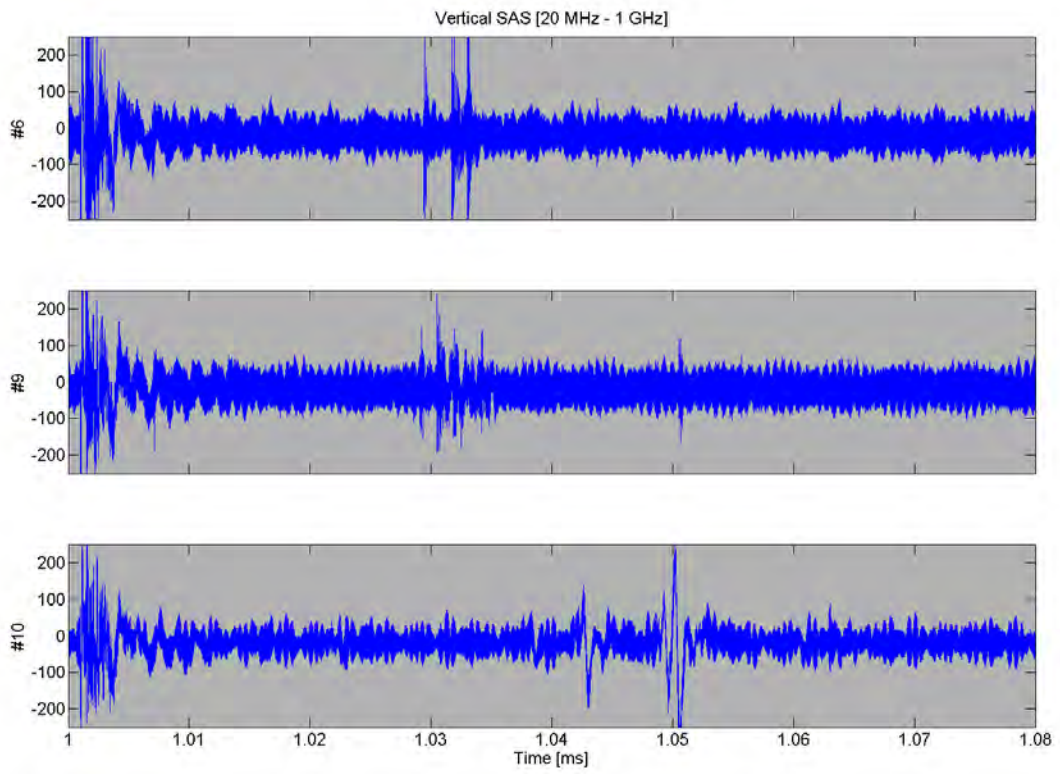


Figure 25. First 80 μ s of Tests 6, 9, and 10, high-frequency antenna. Note that the 3 μ s feature seen in the above ground tests is absent in Test 10, replaced by a slower feature at 40-50 μ s.

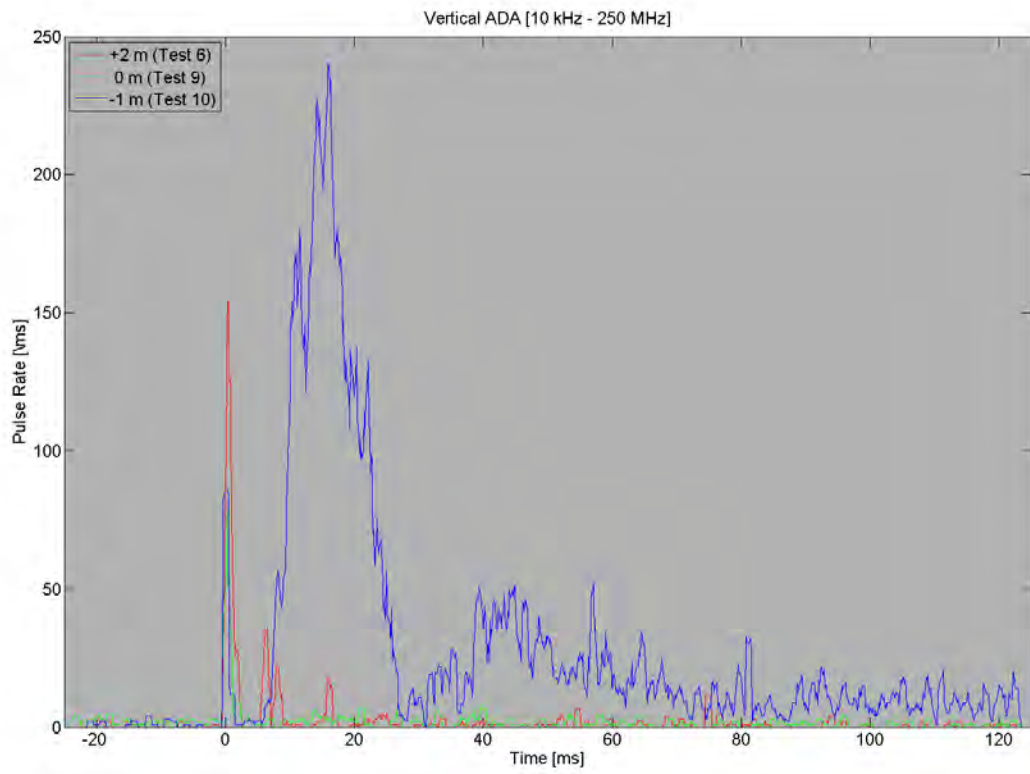


Figure 26. Rate Plot for Tests 6, 9, and 10, low-frequency antenna. The underground detonation produced greatly enhanced levels of low-frequency RF emission.

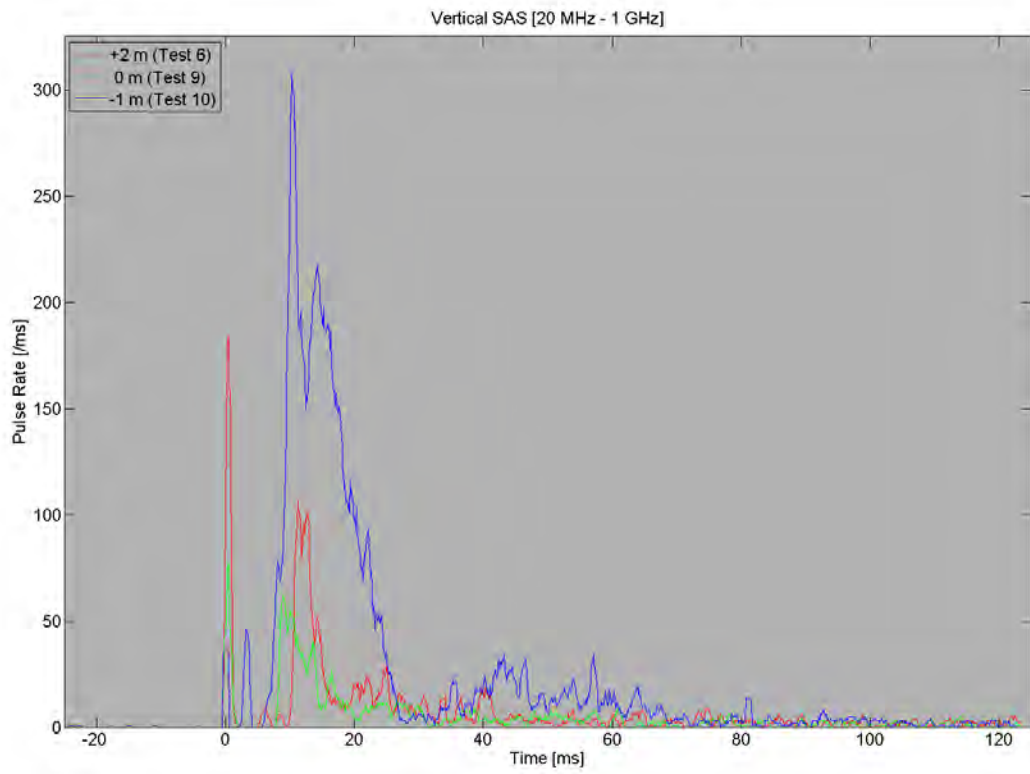


Figure 27. Rate Plot for Tests 6, 9, and 10, high-frequency antenna. The underground detonation produced enhanced levels of high-frequency RF emission.

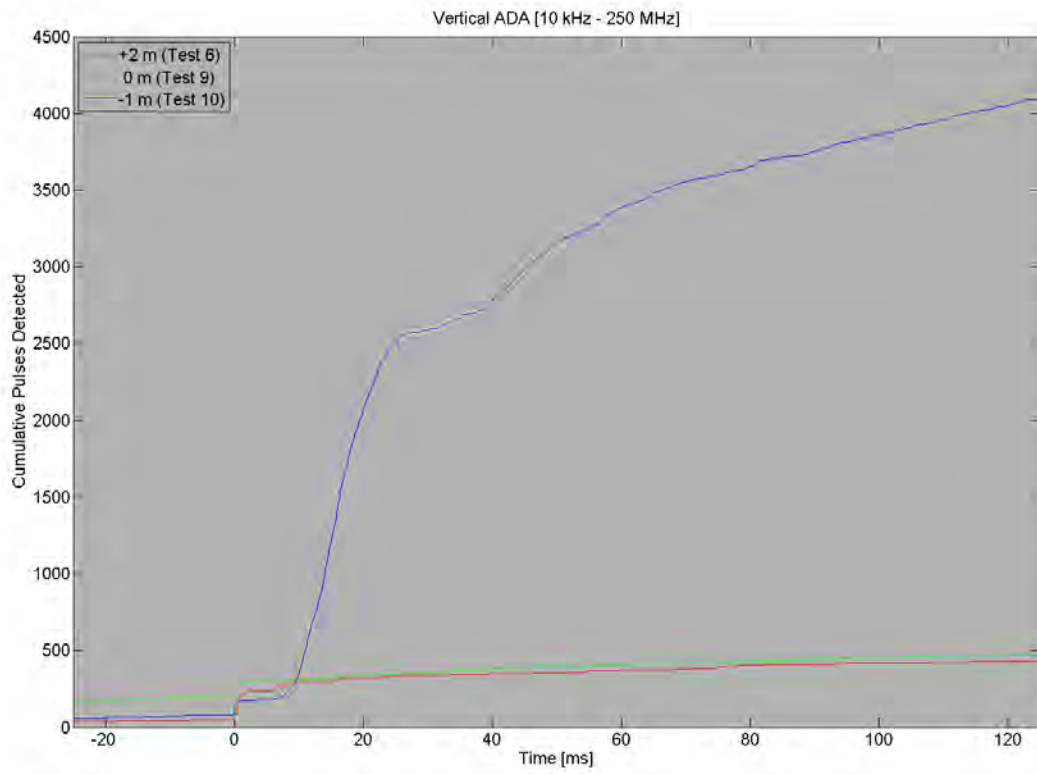


Figure 28. Cumulative pulse counts for Tests 6, 9, and 10, low-frequency antenna; only the T-25 ms to T+125 ms is shown.

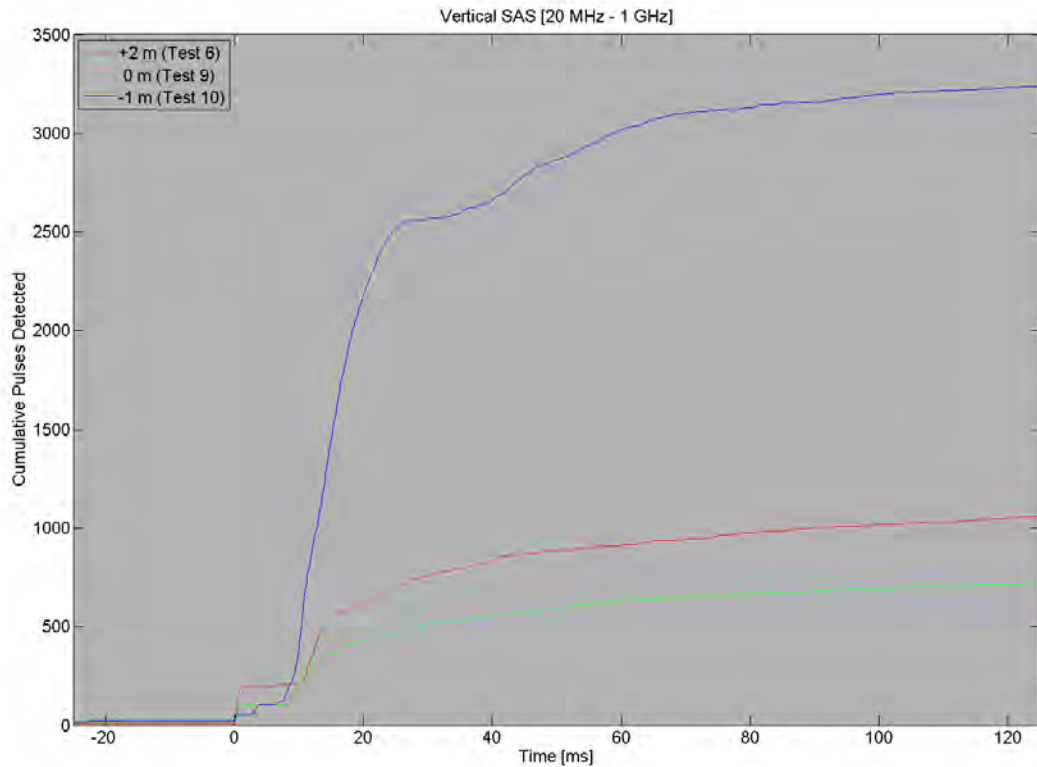


Figure 29. Cumulative pulse counts for Tests 6, 9, and 10, high-frequency antenna; only the T-25 ms to T+125 ms is shown.

Analysis of Seismoacoustic data

Near-field data (< 1 km)

The seismoacoustic sensor deployments at LOSLT and LOSL were at approximately 0.17 and 0.31 km from the shot point respectively. At both sites, similar features were observed on both the acoustic and seismic sensors. The main characteristics of these recordings are summarized here. The acoustic record (see Figure 30) clearly shows that the waveforms from the 8 table shots and the single surface shot are very similar, with high self-similarity extending well into the coda (> 0.7 s) and likely representing similar reflections off canyon walls. The differences between these 9 shots are mainly in terms of the amplitude, as is also observed at more distant stations (see discussion below). In contrast with what we expected, the surface shot cannot be distinguished from the table shots on the basis of the acoustic signal. However, the buried shot can clearly be separated on the basis of a much lower acoustic amplitude (this is expected from the tamping effect of the overburden) and from the delay time of the peak amplitude relative to the above ground shots. The relative delay time of the buried shot is not completely understood at this time. For a shot buried at 1 m in soft alluvium and assuming an acoustic wave speed for the whole path (an underestimate of the average wave speed given nonlinear effects in the near source), the difference in arrival time should be $1/340 = 0.003$ s, which is a full order of magnitude lower than the observed relative delay

time (~ 0.03 s). Interestingly, the same relative delay time is observed at LOSL, which rules out a timing error specific to the individual station.

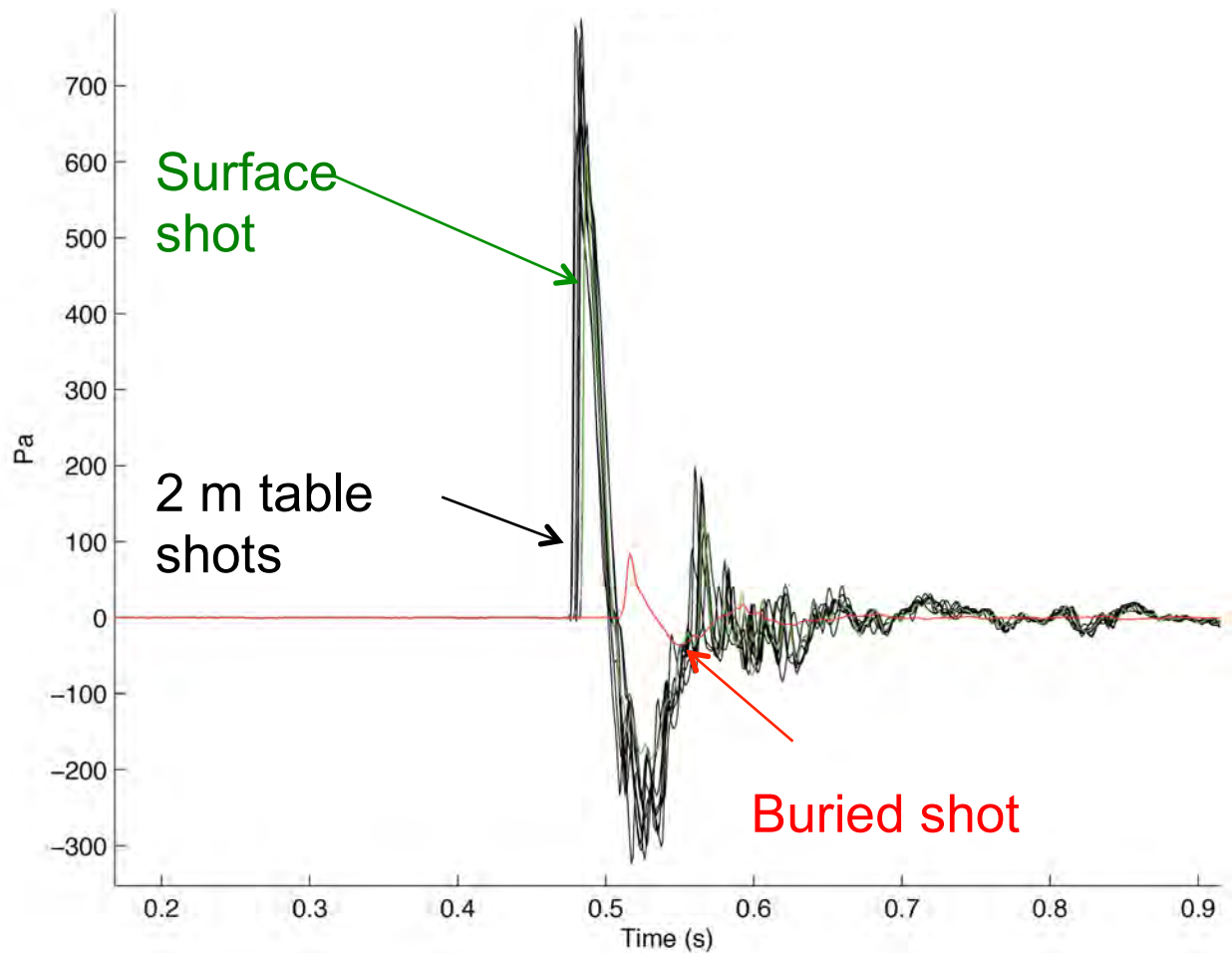


Figure 30. Acoustic signals recorded at LOSL at a distance of 0.17 km. The waveforms are aligned on the shot origin times determined from the RF signals. Black lines represent the 8 identical table shots, the green line represents the surface shot, and the red line represents the buried shot.

The acoustic signals at LOSL were very similar to LOSLT, with the same general conclusions drawn. However, at LOSL we also measured seismic signals, which are shown in Figure 31. The seismic signals exhibit more complexity than the acoustic signals, with several distinct phases observed. However, the same general conclusions can be drawn as for the acoustic signals: similar waveform shapes for the 8 identical table shots, no distinguishing characteristics of the surface shot, and a clearly different character for the buried shot with a reduced amplitude at the acoustic arrival and enhanced amplitudes for seismic surface waves.

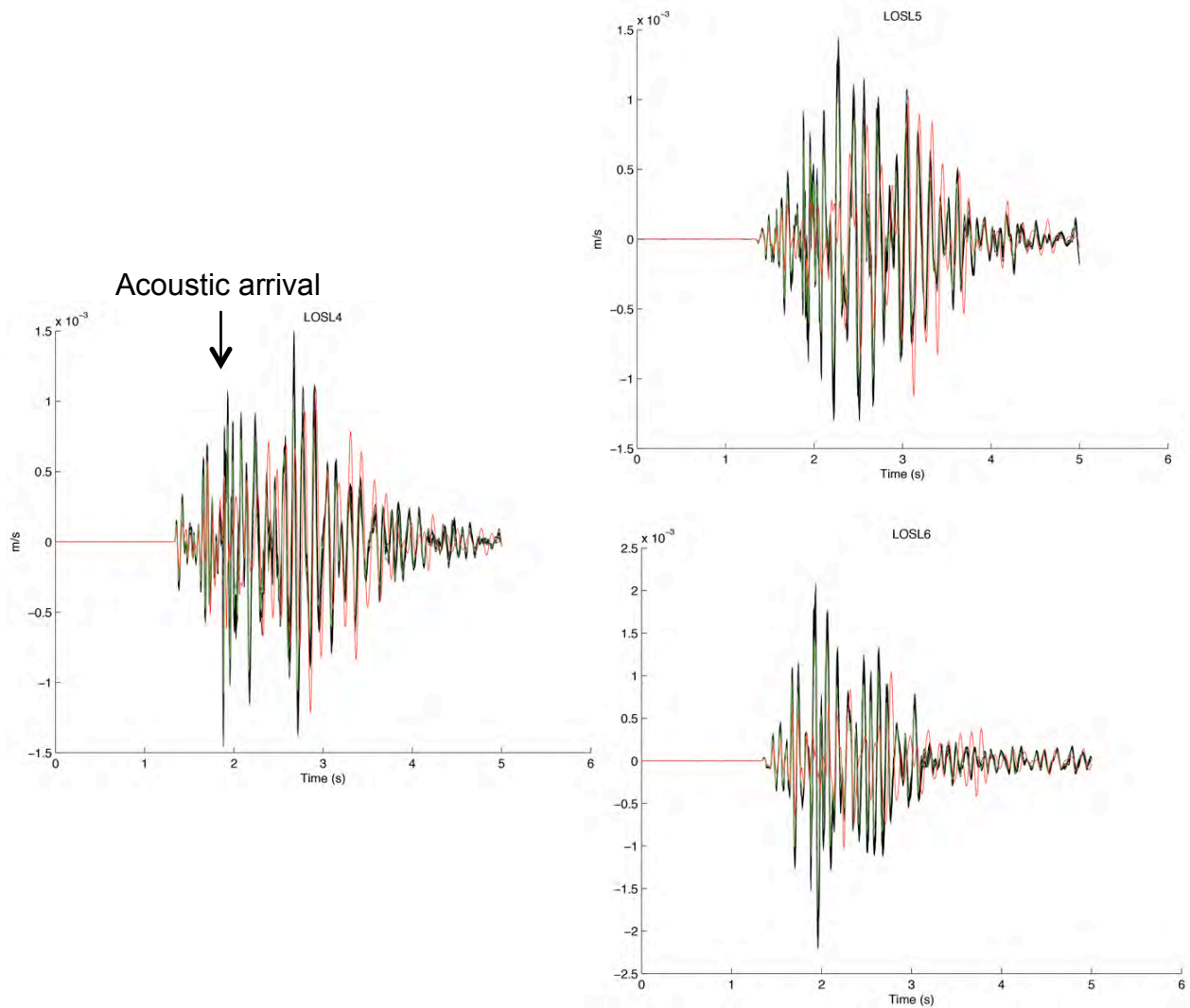


Figure 31. Seismic signals recorded at LOSL, at a distance of 0.36 km. The left panel shows the vertical-component seismic channel, the top right panel shows the north-component seismic channel, and the bottom right panel shows the east-component seismic channel. As in Figure 30, black lines represent the 8 identical table shots, the green line represents the surface shot, and the red line represents the buried shot. The arrival time of the acoustic arrival is shown, at ~ 1.9 s on each plot.

Local data (1 - 3 km)

The acoustic data recorded out to 3 km, at DMOE and PLDY (Figure 9) shows high correlations between the waveforms recorded at these distances (Figure 32). The differences in amplitudes for the 8 identical tests are huge, however, up to about a factor of 5. These observations have important implications for both the discrimination and yield estimation problems. For the discrimination problem the results show that local meteorological effects provide little waveform distortion. However, for the yield estimation problem, the effect of amplitude must be explored further. The dense network of meteorological towers surrounding the LANL firing sites (Figure 9) enables us to explore this in some detail, as discussed below. The seismic observations at PLDY show similar patterns to the near-field seismic data, although in this case the peak arrivals are clearly associated with the acoustic waves.

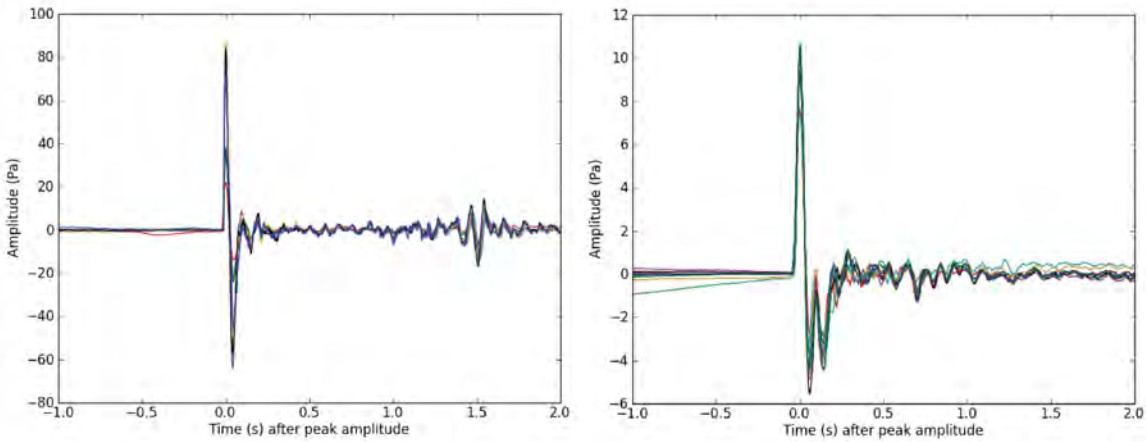


Figure 32. Acoustic signals from the 8 identical table shots at DMOE (left panel) and PLDY (right panel). Different colors represent different shots. Note that the distances from the shot are 1.4 km and 2.7 km respectively.

Relationship of acoustic amplitudes with meteorological data

Acoustic amplitudes recorded remotely are a function of both the source amplitude and the transmission loss (TL) caused by propagation. To first order, one can characterize the atmosphere in terms of its refracting effect on waves, which is a geometric effect and can either enhance or reduce the TL from source to receiver. Also to first order, one can make the effective sound speed assumption, which treats the sound speed profile as a vector sum of the adiabatic sound speed and wind speed in the direction of propagation. The effective sound speed assumption is written as,

$$c_{\text{eff}} = \sqrt{\gamma RT} + \mathbf{v} \cdot \mathbf{n} ,$$

where γ and R are constants, \mathbf{v} is the wind vector and \mathbf{n} is the unit normal vector in the direction of propagation. The effective sound speed can be calculated for a given source-receiver combination using the LANL meteorological tower data. For PLDY, which is upwind, there is a high correlation ($R^2 = 0.98$) between the gradient of the effective sound speed profile, measured at the co-located wind tower, and the amplitude of the acoustic arrival (Figure 33). This result has critical implications for the yield estimation problem as it indicates that the combined effect of winds and temperatures on local-scale paths (~ 3 km) can effectively be removed *for an upward refracting atmosphere*.

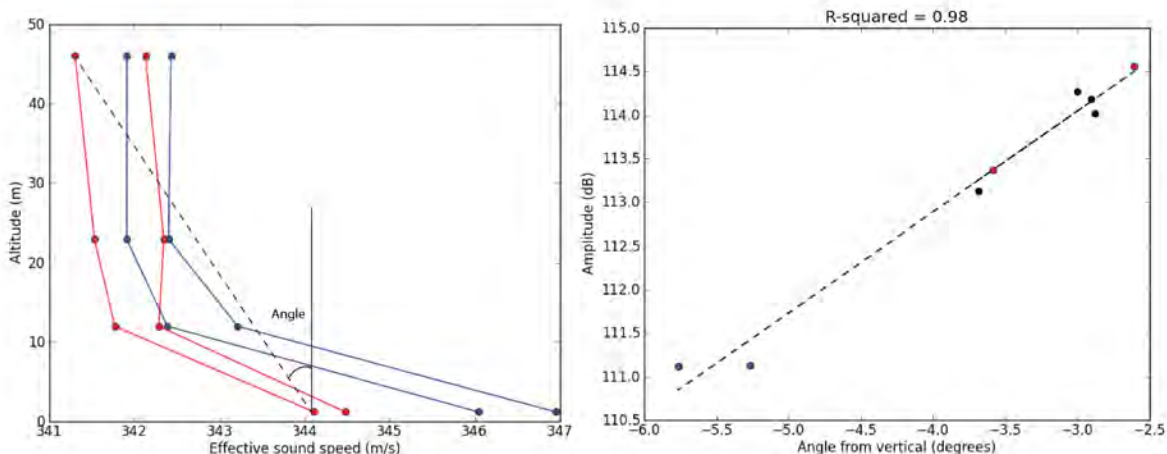


Figure 33. Characterizing meteorological effects on acoustic amplitudes at local distances. The left panel shows the effective sound speed as a function of height from the TA54 meteorological tower for four example events (red and blue colors are for comparison with the right panel). The right panel shows the relationship between the angle from the zenith of the effective sound speed profile and the acoustic amplitude in decibels recorded at PLDY. Black points represent explosions not denoted by sound speed profiles in the left panel.

Our acoustic measurements at DMOE (see map on Figure 9) suggest that downwind propagation is more complex. In our case, downwind propagation leads to an effective sound speed profile that increases as a function of height, refracting sound downwards. This effect should promote refraction of sound in that direction, enhancing amplitudes. Conceptually, a greater positive angle from the vertical should enhance the amplitudes, but we see the opposite trend with $R^2 = 0.79$ (Figure 34). This observation is suggestive of a complex nonlinear relationship between the meteorological profile and topography: the path to DMOE is characterized by a steep cliff face between source and receiver; our hypothesis is that trapping energy with strong positive effective sound speed profiles blocks the sound from reaching DMOE because it reflects off, or diffracts around, the cliff face. In contrast, less energy trapped by the cliff face results in more energy that can reach the sensor. The relatively strong relationship between sound speed gradient and amplitude supports this theory, but indicates that it may be necessary to model both meteorological and topographic effects simultaneously to properly account for these effects *in a downward refracting atmosphere*.

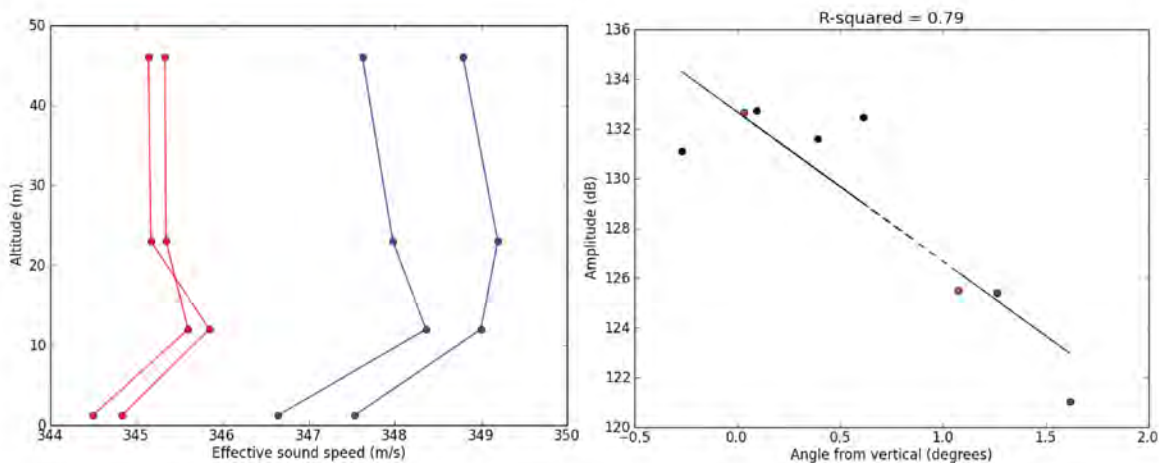


Figure 34. Characterizing meteorological effects on acoustic amplitudes at local distances. The left panel shows the effective sound speed as a function of height from the TA54 meteorological tower for four example events (red and blue colors are for comparison with the right panel). The right panel shows the relationship between the angle from the zenith of the effective sound speed profile and the acoustic amplitude in decibels recorded at DMOE. Black points represent explosions not denoted by sound speed profiles in the left panel.

Discussion

Radiofrequency observations

In comparisons of the eight identical tests, we find several repeating features, and can posit reasons for the origin of most of them:

1. **CDU Pulse:** Occurring at T+0, this pulse is short, with a complicated but very repeatable signature. We presume that the specific waveform is related to the fireset, the characteristics of the detonator cable (length, resistance, inductance, and capacitance), and the bridgewire.
2. **“30 μ s”:** All tests show activity here; given its correspondence with the start or electric field activity predicted by the detonation/plasma model, we presume that this is its origin. The apparent rapid decay of the pulse rate may be due to the effect of the plywood shot stand on the shock wave temperatures and pressures.
3. **“1 ms”:** All tests have a region of emission between T0 and T+2 ms. The amount and precise timing of the start and end of these emissions varies with test. Each test shows a distinct feature that occurs between 400 μ s and 800 μ s. The earliest of these times is coincident with the calculated arrival time of the expanding shock wave, so we assume that this feature is the same as the ground contact pulse seen in other tests, with a variability imposed by the plywood shot stand. We currently assume that this emission is due to shorting of ionization engendered by detonation or combustion of detonation byproducts, or by a piezoelectric effect.
4. **“5 ms”:** several tests seem to show a small amount of emission roughly between T+5 ms and T+7 ms; it is not clear whether this is a separate population, or what causes it. It may simply be a precursor of the “10 ms” emission feature. AN alternative view is that this relatively small feature could be due to combustion ionization.

5. “10 ms”: Most of the RF occurs in the large region that starting at 6-8 ms and peaking around 10 ms, continuing at low level for the rest of the useable record. It changed regularly from test to test, becoming both earlier and larger, making us hypothesize that it involves the ground, and changed as the ground became either more compacted, more pulverized, or drier through the action of each successive detonation. This feature (or something coincident with it) is greatly enhanced in the “underground” detonation (Test 10), especially in the low frequencies. We assume therefore, that it is due to the charging of dust, dirt, and debris from the action of the explosion. In the +2 m and 0 m tests this is presumably due to frictional charging in collisions; in the -1 m test, rock fracturing may also be involved.

In Figures 35 and 36, we show summary rate plots annotated with our hypothesized sources for RF in various temporal regimes. In each Figure, the lower plot consists of Tests 2 through 8 superimposed, while the upper plot consists of Tests 2 through 8 averaged together. RF caused by the high-temperature ($\sim 10000\text{K}$) detonation shock wave dominates from $\sim 30\ \mu\text{s}$ $\sim 400\ \mu\text{s}$, as the shock cools down to $\sim 4000\ \text{K}$ [scaled from results published by Kuhl, 2012]. Then, upon ground contact (400-800 μs , depending on test), the RF generation rate increases abruptly for a short period. By 2 ms, most of the RF generation has subsided, and the rates remain low until ~ 5 ms. After a short bursts of radiation in some tests, the main region of RF generation starts (8-16 ms, test-dependent), due to the entrainment and charging of dust.

At this point, we do not see distinct features in the data that we can ascribe to combustion. Assuming typical combustion temperatures (2000 K), we expect that any radiation due to combustion-ionization would be at rates lower than we see at T+300 μs , in the 4000 K and cooling shock front. Of course, the larger volume presumably involved in combustion region compared to the detonation shock may partially reverse the low ionization expected in the relatively cool combustion regime. Thermal ionization is exponential in temperature, so even factors of two in temperature reduction can have large effects on relative ionization. We also note that the T+2-5 ms gap in RF production may constrain estimates of RF from combustion: if combustion is occurring during that interval, it cannot be producing much RF. The small feature around 5 ms is a potential signature of ionization from combustion.

One result that appears anomalous is the lower level of radiation emanating from the 0-m case compared to the +2-m case. The +2-m detonations created less obvious dust as seen in video recordings of the tests and no obvious craters, compared to the 0-m test, which created a crater as defined above. So we would expect a greater 10-ms peak in Test 9 data. The explanation may lie in the shock geometry, which would have been primarily a downward impulse for Test 9, as opposed to a more oblique force for the elevated tests. This could have been more effective at “sweeping” dust particles along the ground and against each other. In addition, sand bags used to hold down the shot stand disappeared during the blast, providing an additional source of dust for the elevated tests. The total RF production in Test 6, the 2-m test depicted in Figure 27, was third-highest of the eight elevated tests.

All of these tests were measured at relatively close range (45 m); therefore, for many pulses the antenna was in the electromagnetic near field. Extension of the results to greater distances must therefore be done with caution. To date, we have not done an analysis of pulse shape/bandwidth as a function of test or emission regime. Given that several physical mechanisms are likely involved, that may be an important next step.

For future tests, some important considerations will be to change the design of the shot stand, to ensure that it doesn't affect the results, testing additional sizes or configurations that can be quantitatively modeled, and trying test designs that will either maximize or minimize the effects of dirt.

Seismoacoustic observations

Based on the seismoacoustic observations presented in this report, the following conclusions can be drawn:

1. Seismoacoustic measurements can clearly discriminate the buried shot from the table and surface shots but cannot distinguish the surface and table shots from each other.
2. Seismoacoustic signals at distances where implosion signatures were observed from NNS tests have highly consistent waveforms, while the amplitudes are highly dependent on the specific atmospheric conditions.
3. Consistent waveforms support the development of a template matching approach for combined detection and discrimination at these distances.
4. Amplitude differences due to meteorological effects can be predicted from these experiments for upward refracting atmospheres and appear to be weakly related to topography.
5. Amplitude differences associated with upward refracting atmospheres suggest a complex interplay between meteorological and topographic effects.

Based on these observations, the future recommendations from the RF perspective are also of relevance to enhancing seismoacoustic capability. In particular, more buried shots and a range of shots with different yields are recommended.

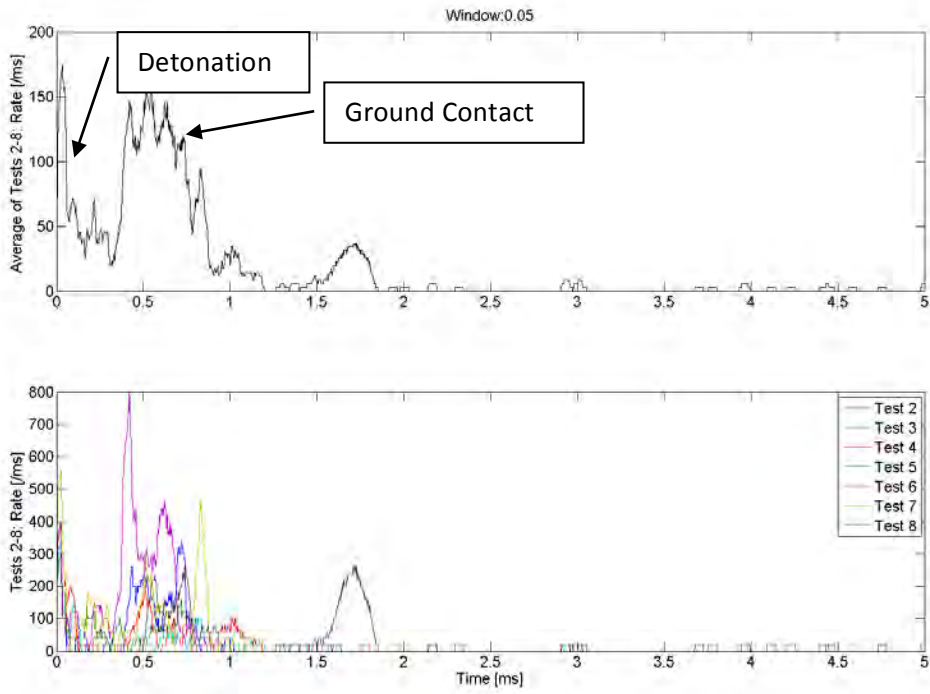


Figure 35. Composite rate plots, first 5 ms

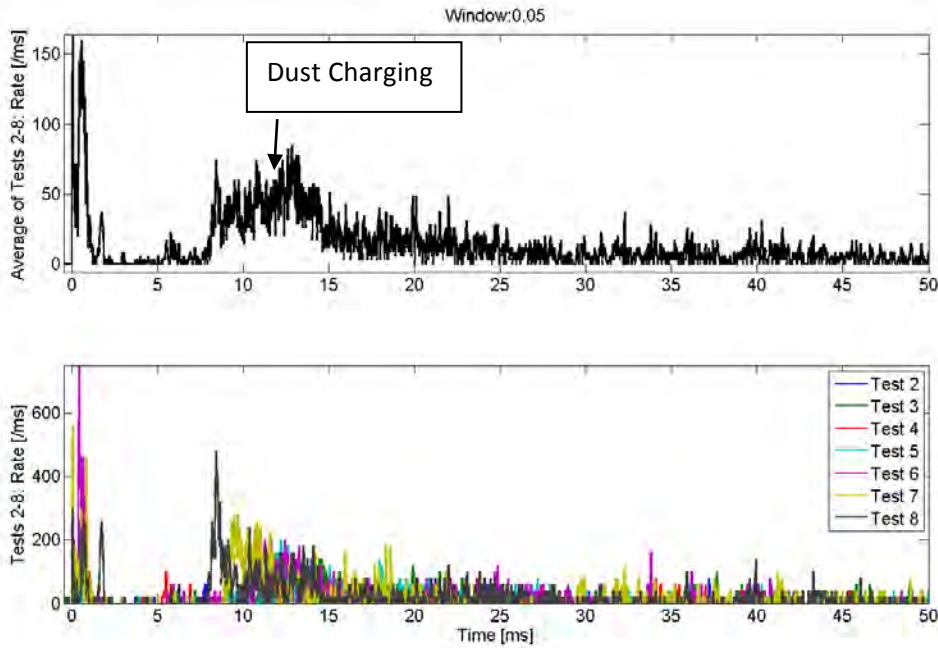


Figure 36. Composite rate plots, first 50 ms